NANO LETTERS

pubs.acs.org/NanoLett

Letter

Room Temperature Dynamics of an Optically Addressable Single Spin in Hexagonal Boron Nitride

Raj N. Patel,[#] Rebecca E. K. Fishman,[#] Tzu-Yung Huang, Jordan A. Gusdorff, David A. Fehr, David A. Hopper, S. Alex Breitweiser, Benjamin Porat, Michael E. Flatté, and Lee C. Bassett[*]

Cite This: *Nano Lett.* 2024, 24, 7623–7628

Read Online

ACCESS | Metrics & More | Article Recommendations | Supporting Information

ABSTRACT: Hexagonal boron nitride (h-BN) hosts pure single-photon emitters that have shown evidence of optically detected electronic spin dynamics. However, the electrical and chemical structures of these optically addressable spins are unknown, and the nature of their spin-optical interactions remains mysterious. Here, we use time-domain optical and microwave experiments to characterize a single emitter in h-BN exhibiting room temperature optically detected magnetic resonance. Using dynamical simulations, we constrain and quantify transition rates in the model, and we design optical control protocols that optimize the signal-to-noise ratio for spin readout. This constitutes a necessary step toward quantum control of spin states in h-BN.

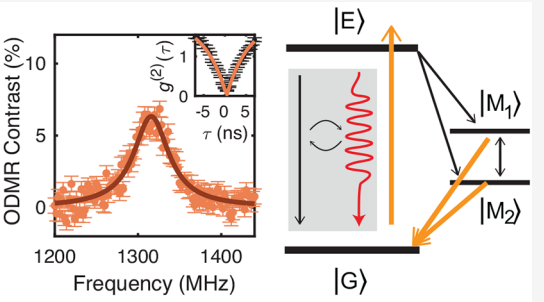

KEYWORDS: *Quantum control, hexagonal boron nitride, time-resolved photoluminescence, spin dynamics, point defects, quantum engineering*

Optically interfaced solid-state spins enable quantum technologies with unprecedented capabilities for sensing,[1−4] communication,[5] quantum-coherent memories,[6,7] and exploration of fundamental physics.[8] Several host materials are available[9] and new ones continue to be explored in search of desirable properties.[10] Hexagonal boron nitride (h-BN), a wide-bandgap semiconductor that hosts numerous species of optical defects, is especially promising for its low-dimensional morphology that facilitates efficient photon collection and device engineering advantages compared to three-dimensional crystals.[11]

Recent observations have confirmed the potential of h-BN as a host for quantum defects. Ensemble measurements have facilitated exploration into the excited-state spin properties of boron vacancies in h-BN.[12,13] On a single-defect level, room-temperature optical emitters in h-BN have shown single-photon emission.[14] Select single emitters further exhibit magnetic-field-dependent photoluminescence (PL), optically detected magnetic resonance (ODMR), and quantum-coherent spin oscillations,[15−19] all of which are prerequisites to establishing optically addressable spin qubits in h-BN.

Despite this progress, paramagnetic single-photon emitters are a minority of those reported on in h-BN, with recent observations noting a measurable ODMR signal in ∼5% of isolated defects.[19] Single emitters in h-BN can exhibit heterogeneous optical and spin properties due to differences in local environment, chemical structure, and sample preparation.[20] Many questions therefore remain about the nature of these emitters. Ultimately, the informed design of spin control protocols that are optimized for applications requires a detailed understanding of their optical and spin dynamics.

In this letter, we investigate an emitter in h-BN that exhibits single-photon emission and ODMR at room temperature. We probe the emitter's optical and spin dynamics using photon emission correlation spectroscopy (PECS)[21] and time-domain optical and microwave control. We develop a model for the emitter's energy-level structure, and determine the rates that govern its optical and spin dynamics using quantitative simulations. We design a readout protocol for the spin state that optimizes the signal-to-noise ratio (SNR).

The sample consists of a mechanically exfoliated h-BN flake (≤100 nm) suspended on a patterned SiO_2/Si substrate.[14,20] In an area of ≈25 × 25 μm^2, only one emitter exhibited magnetic-field-dependent PL, among ≈20 nonmagnetic emitters. We characterize the emitter's optical dynamics under ambient conditions using a confocal microscope.[14,21] The emitter is illuminated with either of two continuous-wave (cw) lasers operating at 532 and 592 nm wavelengths, where excitation power and polarization are controlled. Data

Received: March 19, 2024
Revised: May 1, 2024
Accepted: May 29, 2024
Published: June 11, 2024

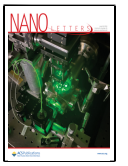

https://doi.org/10.1021/acs.nanolett.4c01333
Nano Lett. 2024, 24, 7623−7628

recorded under 592 nm (532 nm) excitation are plotted in orange (green) in the relevant figures.

Figure 1(a) shows the emitter's PL spectrum under 532 nm excitation. The excited state lifetime is found to be 7.8 ns through PECS analysis (Supporting Information (SI), Sec. 4.3). The emitter's optical excitation is highly polarized (visibility 93 ± 3%) and aligned for both 532 and 592 nm excitation (Figure 1(b)). The emitted PL is polarized along the same axis (SI, Figure S4). While previous observations have noted heterogeneous polarization responses for h-BN's emitters,[14,20,22−24] indicating the presence of multiple electronic excited states, the aligned excitation and emission dipoles observed for this emitter are consistent with a single radiative excited state. Figure 1(c) shows the second-order photon autocorrelation function, $g^{(2)}(\tau)$, at zero-delay ($\tau = 0$). After accounting for experimental uncertainties (SI, Sec. 3.2), we observe noise-limited photon antibunching, $g^{(2)}(0) = 0$, independent of optical excitation power in the presence and absence of an applied magnetic field.

This emitter's PL intensity is modulated by applied dc and ac magnetic fields. Magnetic fields affect a paramagnetic defect's PL intensity due to spin-selective transition rates that govern its optical dynamics, although this can occur in different ways.[16,21,25,26] We apply a dc magnetic field parallel to the hBN surface and rotate the sample about the optical axis to vary the relative orientation of the optical excitation dipole to the field axis (referred hereafter as dipole orientation). As observed in Figure 1(d), the steady-state PL varies by 15% on increasing the magnetic field strength from 0 to 470 G for both 0° and 15° dipole orientations. Accompanying variations in PECS measurements confirm that the PL changes result from magnetic modulation of the emitter's optical dynamics (SI, Figure S5). Figure 1(e) shows an example of an ODMR spectrum acquired as a function of applied microwave frequency. The microwaves are amplitude modulated at 12.5 kHz, and the ODMR spectrum is normalized by dividing the signal PL (microwaves on) by the reference PL (microwaves off).

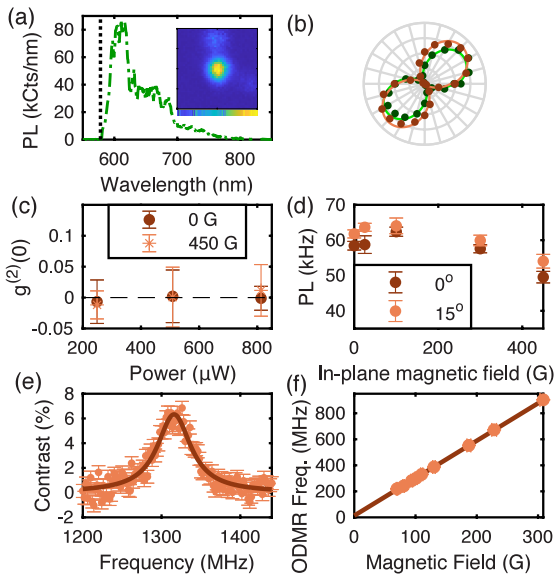

Figure 1. Optical characterization and ODMR. (a) PL emission spectrum. The black dotted line represents the cut-on wavelength of a long-pass dichroic filter in the collection path. Inset: μ-PL image (2 μm × 2 μm) of the single spin. The color scale ranges from 0 (blue) to 41 (yellow) kcts/s. (b) PL intensity as a function of linear excitation polarization angle for 532 nm (green circles) and 592 nm (orange circles) excitation. Solid curves are fits to the data. (c) Optical-power-dependent $g^{(2)}(0)$ for two different in-plane magnetic fields at 0° dipole orientation. (d) Time-averaged PL emission as a function of an in-plane magnetic field for 0° and 15° dipole orientation. (e) Continuous-wave ODMR spectrum (circles) at 470 G applied magnetic field and 0° dipole orientation. A Lorentzian fit (solid line) gives a resonance frequency of 1315.9 ± 0.8 MHz and a full-width half-maximum of 52 ± 2 MHz. (f) Spin resonance frequency as a function of magnetic field, measured using a pulsed ODMR protocol. The solid line is a linear fit to the data. Uncertainties in field and frequency are similar size to the data points. Error bars for (e) are propagated from Poissonian uncerrtainties. All other error bars represent 68% confidence intervals.

Figure 1(f) shows a linear fit to the best-fit ODMR center frequency as a function of applied magnetic field at 1.8° dipole orientation. We repeat this measurement for 34.2°, 66.6° and 90° dipole orientation (SI, Figure S12) and find an isotropic Landé g-factor, $g \approx 2$, consistent with the free-electron g-factor, and an average zero-field-splitting (ZFS) of 9 ± 10 MHz. Given the order of magnitude of the ZFS and its consistency with zero within experimental uncertainty, we interpret this as an absence of ZFS. The scale of the ZFS agrees with prior reports, although interpretations of its significance have varied (SI, Sec. 6.2).[18,19] We observe no additional resonances at higher frequencies up to 4.2 GHz. Thus, we postulate a doublet ($S = \frac{1}{2}$) spin state. However, we acknowledge higher-level spin configurations, while less likely, are possible (SI, Sec. 6.3).

Figure 2(a) shows the proposed model explaining the observed optical dynamics. The model features a metastable spin-1/2 doublet ($|M_{1,2}\rangle$), coupled to a spinless manifold of ground ($|G\rangle$) and optically excited ($|E\rangle$) states. We identify a stochastic modulation of the optical decay pathway, fluctuating between a raditative and nonradiative transition. Arrows denote transitions with corresponding rates, k_{ij}, between states i and j, with the spin relaxation rate labeled T_1^{-1}. The number and arrangement of levels are determined by a series of experiments and corresponding simulations. PECS measurements (discussed later), show clear evidence of photon bunching associated with metastable dark configurations and reveal the nature of the transition mechanisms between these configurations.[21] In addition to the optical excitation transition rate, k_{GE}, PECS simulations imply that the rates k_{M_1G} and k_{M_2G} each feature a power-dependent component in addition to a spontaneous (power-independent) component (SI, Sec. 3.3).

We propose that the spin doublet state observed in ODMR exists in a metastable configuration. This arrangement cannot be determined by ODMR alone. Rather, it is confirmed by an optical spin contrast experiment, shown in Figure 2(b-c), which distinguishes between configurations where the spin states exist in the optical excitation/emission manifold compared to the metastable configuration. As shown in Figure 2(b), the laser is modulated on and off, with a dark time of duration τ_D, and a microwave pulse can be applied during the dark time following a wait time, τ_w. Figure 2(c) shows the PL as a function of time during the laser pulse in situations when the microwaves are applied (signal) or not (reference).

We consider in turn the expected dynamics for configurations with spin doublets in the optical ground and excited states compared to the configuration shown, with a metastable

https://doi.org/10.1021/acs.nanolett.4c01333
Nano Lett. 2024, 24, 7623−7628

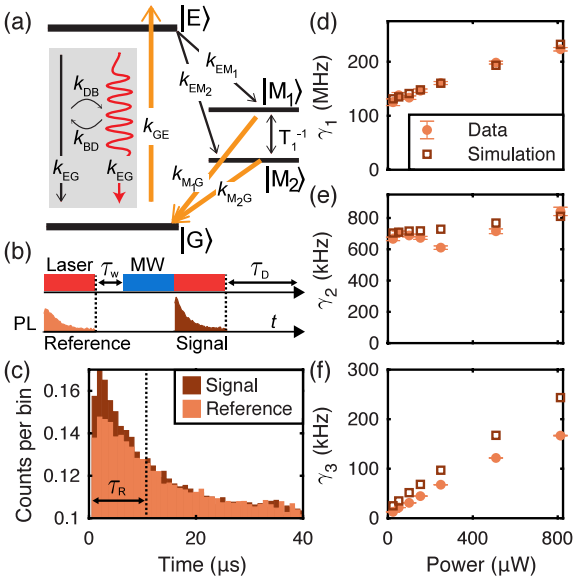

Figure 2. Energy-level model and optical dynamics. (a) Energy-level model made up of a singlet ground and excited state, and a metastable doublet. The gray box highlights fluctuations between a nonradiative decay path (black arrow) and radiative decay (red, wavy arrow). Orange arrows depict excitation-power-dependent transitions. (b) Pulse protocol for optical spin contrast measurements. "Reference" and "Signal" denote timing windows during which photons are counted. (c) PL counts in 1 μs time bins corresponding to signal (dark orange bars) and reference (light orange bars) readout, at 350 μW optical power, 470 G magnetic field, 20 μs wait time, and 40 μs microwave pulse time. The dashed line indicates the approximate time contrast disappears, denoting a readout window. (d)−(f) PECS measurements. The rates(d) γ_1, (e) γ_2, and (f) γ_3 are shown as a function of optical excitation power at 0 G magnetic field.

doublet. The former case (spins in optical manifold) would predict zero initial spin contrast when the laser is turned on, with a contrast evolving during the pulse due to spin-dependent decay rates, whereas the latter configuration (metastable spin) predicts a nonzero initial contrast that decays as the system returns to the steady state (SI, Sec. 5.1). Our observations are consistent with the latter case. This finding and the power-dependent transitions from the metastable state could indicate a transition between charge manifolds, similar to the NV-center transition between NV^- ($S = 1$) and NV^0 ($S = \frac{1}{2}$).[25] Informed by classical rate equation simulations of a spin contrast experiment for the model shown in Figure 2(a), we estimate a maximum spin relaxation rate of $T_1^{-1} \sim 0.01$ MHz to achieve a similar initial contrast (7%) in simulations.

After establishing the main features of the electronic level structure, we next consider the rates that govern its optical dynamics. Using PECS, we acquire $g^{(2)}(\tau)$ at various optical excitation powers. To analyze the data, we follow the procedure from previous works (see ref.[14]), evaluating the Akaike information criterion and reduced chi-squared statistics for n-time scale models. We determine the best-fit empirical function to be a three-time scale model,

$$g^{(2)}(\tau) = 1 - C_1 e^{-\gamma_1|\tau|} + C_2 e^{-\gamma_2|\tau|} + C_3 e^{-\gamma_3|\tau|} \quad (1)$$

where τ is the delay time, γ_1 and C_1 are the antibunching rate and amplitude, γ_2 and γ_3 are the bunching rates, and C_2, C_3 are the associated bunching amplitudes. Both γ_1 and γ_3 increase monotonically as a function of optical excitation power (Figures 2(d) and 2(f)), as expected for processes involving optical pumping to the excited state. In contrast, γ_2 shows no clear trend with respect to power (Figure 2(e)).

Each PECS rate originates from transition pathways between multiple electronic states that define a distinct process. In this model, γ_1 corresponds to optical excitation at rate k_{GE} followed by relaxation back to $|G\rangle$ at rate k_{EG}. For a direct optical transition between two electronic states, as in this model, the antibunching rate is given by $\gamma_1 \approx k_{GE} + k_{EG}$.[21,27] The observations in Figure 2(d) reflect the expected linear power-dependence of k_{GE} with a nonzero y-intercept equivalent to k_{EG} (SI, Sec. 4.3).

The bunching rates γ_2 and γ_3 represent processes through which the system enters nonradiative configurations. The power-dependence of γ_3 is consistent with the process of optical excitation to $|E\rangle$ at power-dependent rate k_{GE}, followed by nonradiative decay through $|M_{1,2}\rangle$ back to $|G\rangle$ at power-dependent rates k_{M_1G} and k_{M_2G}. In contrast, γ_2 does not vary significantly with optical excitation power, p. To account for this, we propose a relaxation mechanism from $|E\rangle$ to $|G\rangle$ that stochastically switches between radiative and nonradiative configurations at rates k_{DB} and k_{BD} through a process independent of p. This mechanism produces blinking, a commonly observed phenomenon in quantum systems consisting of periods of reduced PL due to charge quenching or fluctuations in the local environment.[28] The power-independence of γ_2 suggests that the emission modulation could be from environmental fluctuations, for example through coupling to the state of a nearby defect. As shown by the simulations in Figure 2(e), this process leads to bunching in $g^{(2)}(\tau)$ at a nearly constant rate $\gamma_2 \sim k_{DB} + k_{BD}$, which closely matches the experimental observations.

PECS analysis yields estimates for the overall rates connecting $|E\rangle$, $|M_{1,2}\rangle$, and $|G\rangle$ through γ_3. However, an analytical expression for γ_3 in terms of transition rates is not straightforward to derive. Therefore, additional measurements are required to resolve the contributions of each individual rate. The fluorescence recovery protocol (Figure 3(a)) involves varying the dark time, τ_D, between laser pulses and recording the time-domain PL emission during each pulse. Figure 3(b) illustrates the evolution of populations in $|G\rangle$ and $|E\rangle$ during a fluorescence recovery experiment for two different values of τ_D. The measured PL (shown in Figure 3(c) for 15 different values of τ_D) is proportional to the population in $|E\rangle$, which depends in turn on the population in $|G\rangle$ at the beginning of the laser pulse. The PL at the start of the laser pulse (dashed line in Figure 3(c)) increases as a function of τ_D, with an extracted time constant of 73 ± 5 μs. During the laser pulse, the PL decays to a steady-state value with a decay constant of 7.9 ± 0.4 μs. The maximum contrast from the initial to the steady-state PL is measured to be 62.2 ± 0.2%. These three features help constrain the metastable transition rates in different ways. The time constant describing the increase in PL at the start of the laser pulse is determined by the power-independent components of k_{M_1G} and k_{M_2G}. The maximum contrast depends on the ratio, $(k_{M_1G} + k_{M_2G})/(k_{EM_1} + k_{EM_2})$. The decay time from maximum to steady-state PL is dependent on many rates but can be leveraged along with the previous constraints to empirically determine a value for k_{EM} through simulations.

https://doi.org/10.1021/acs.nanolett.4c01333
Nano Lett. 2024, 24, 7623−7628

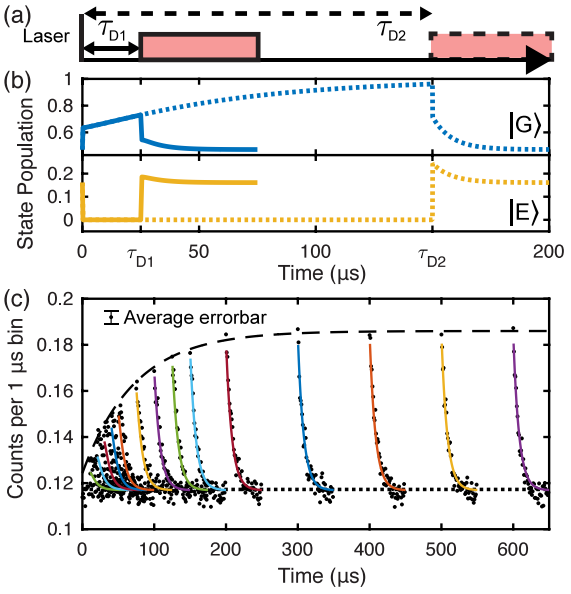

Figure 3. Fluorescence recovery. (a) Pulse protocol for the time-domain fluorescence recovery measurement. (b) Example of time-domain ground (blue lines) and excited (yellow lines) state populations during a fluorescence recovery experiment for short (τ_{D1}) and long (τ_{D2}) dark times between laser pulses, shown as solid and dashed lines, respectively. (c) Time-domain PL as a function of dark time between optical pulses, τ_D, acquired at 91 G in-plane magnetic field and 34.2° dipole orientation, using 1 μs time bins. Black dots are data, and colored lines are simulation. The average uncertainty of each data point is ±0.003 counts per bin.

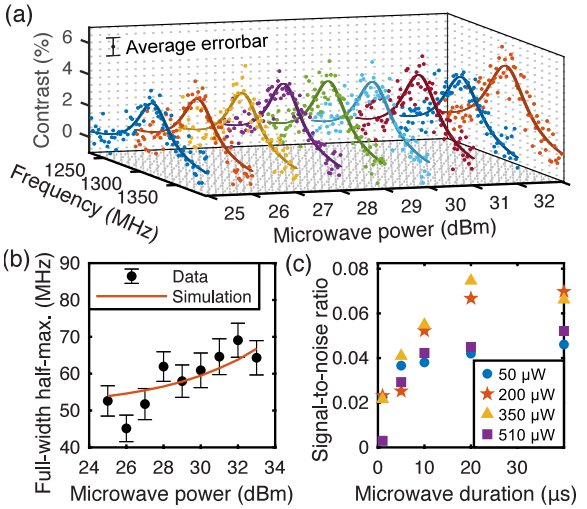

Figure 4. Spin properties. (a) ODMR data (points) with simulation fits (lines) as a function of microwave frequency and power. The average uncertainty of each data point is ±0.5%. (b) ODMR full-width half-maximum as a function of microwave power, extracted from Lorentzian fits to the simulation and data. (c) Signal-to-noise ratio as a function of microwave pulse duration for readout time, τ_R = 5 μs, at varying optical powers. All data are acquired at 592 nm excitation and 470 G magnetic field.

We use a rate equation model for the level configuration shown in Figure 2(a) to numerically simulate the state populations for PECS and the fluorescence recovery pulse protocol (SI, Sec. 4). The parameters k_{EG} and k_{GE} are known based on earlier considerations, as is the sum $k_{DB} + k_{BD}$. We determine the remaining parameters by empirically matching simulations of PECS rates (squares in Figure 2(c-e)) and bunching coefficients (SI, Figure S8), spin contrast (Figure 2(c)), and fluorescence recovery PL (colored lines in Figure 3(c)) to the data. The simulated fluorescence recovery time constants match those extracted from the data within fit errors, and the maximum contrast matches within 5%. Discrepancies between the PECS simulations and data are attributed to variations of the spin-dependent rates through $|M_{1,2}\rangle$ due to different applied magnetic fields for the PECS (no field) and fluorescence recovery (91 G) experiments. The power-independent k_{M_1G} and k_{M_2G} components set an upper limit of ~30 μs on the metastable spin's useful lifetime. The optimized rates and details on the process of quantifying them can be found in SI Sec. 4.3.

We model the ODMR experiments using the Lindblad framework to capture coherent evolution of the spin states along with semiclassical optical dynamics.[29] Our experiments indicate a variation of the ODMR contrast and line width as a function of microwave power, p_{MW} (Figure 4(a)). We fit Lindblad simulations to these data, using the optimized optical-dynamics rates as fixed parameters. Free parameters include the microwave coupling efficiency, η, which determines the power-dependent Rabi frequency according to $\Omega_R/(2\pi) = \eta\sqrt{p_{MW}}$, as well as the spin dephasing time, T_2^*. The fits are plotted along with the data in Figure 4(a), and Figure 4(b) compares the ODMR line width extracted from the data to the best-fit simulation. Accounting for uncertainties in the fit and in T_1, we find η = 0.0189 ± 0.0007 MHz/$\sqrt{\text{W}}$ and T_2^* = 6.3 ± 0.1 ns (SI Sec. 4.4).

Using this quantitative understanding of the emitter's optical dynamics, we can design optimized protocols for spin initialization and readout. Spin polarization develops under optical illumination due to the spin-dependent branching ratios k_{EM_1}/k_{EM_2} and k_{M_1G}/k_{M_2G}. Our model implies a steady-state population ratio $|M_2\rangle$:$|M_1\rangle$ ~ 30:1 at p = 350 μW. The corresponding spin polarization ~97% significantly exceeds the steady-state polarization for other spin defects such as the diamond nitrogen-vacancy (NV) center. However, the population develops over ~10 μs, which is an order of magnitude longer than typical NV-center initialization times.[30] To optimize spin readout, we consider the single-shot SNR in a spin contrast experiment (Figure 2(b)),[30]

$$\text{SNR} = \frac{\alpha_1 - \alpha_0}{\sqrt{\alpha_1 + \alpha_0}} \tag{2}$$

Here α_1 and α_0 are, respectively, the mean number of detected photons for the signal (microwave on) and reference (microwave off) recorded in a given readout window, τ_R (Figure 2(c)). Figure 4(c) shows the SNR as a function of microwave pulse duration, for various settings of p. We find an optimum SNR ≈ 0.07 for p = 350 μW and τ_R = 5 μs. Since the spin contrast experiment in Figure 2(b) compares the polarized spin configuration with a fully mixed state, the observed SNR is approximately half of what would be expected for a full spin inversion. For comparison, the optimized spin-readout SNR for a diamond NV-center with similar photon count rate is only ~0.03.[30] The spin contrast's persistence over an order of magnitude longer than in the NV-center, contributes to a $\sqrt{10}$-times-increase in SNR.

The quantitative model presented in this work will directly facilitate the use of single spins in h-BN for quantum

https://doi.org/10.1021/acs.nanolett.4c01333
Nano Lett. 2024, 24, 7623−7628

technologies. The inferred spin polarization of ∼97% and spin-readout SNR of ∼0.15 are superior to the performance of well-established room-temperature spin qubits, including NV centers. More sophisticated initialization and readout protocols could offer further improvements.[30] The spin relaxation time, $T_1 \approx 100\ \mu s$, is comparable to the spin lifetimes of NV centers in nanodiamonds. The effective spin lifetime of ∼30 μs offers opportunities for relaxometry imaging and chemical sensing. The spinless ground state configuration can be beneficial to protect the coherence of nuclear spin states.[31] The relatively short dephasing time, $T_2^* = 6.3 \pm 0.1$ ns, likely reflects substantial hyperfine coupling to nearby nuclear spins. Hence, with the design of optimized microwave antennas to drive faster spin rotations, it will be possible to use dynamical decoupling protocols to substantially extend the electron-spin coherence time, and to address the states of coupled nuclear spins.

The chemical structure of h-BN's visible emitters remains a mystery. Conclusive identification is needed to enable the further optimization of materials, devices, and quantum control protocols. The detailed empirical understanding of their energy-level structure and dynamics developed through this work will inform and constrain future theoretical models. More generally, the framework followed in this letter can be used to characterize and control the optical and spin dynamics of single spins in any solid-state host material.

■ ASSOCIATED CONTENT

Supporting Information

The Supporting Information is available free of charge at https://pubs.acs.org/doi/10.1021/acs.nanolett.4c01333.

Details on sample preparation and experimental setup; additional polarization, PECS, and ODMR measurements; additional SNR calculations; simulation details; and discussion of previous reports of single spins in h-BN (PDF)

■ AUTHOR INFORMATION

Corresponding Author

Lee C. Bassett − *Quantum Engineering Laboratory, Department of Electrical and Systems Engineering, University of Pennsylvania, Philadelphia, Pennsylvania 19104, United States;* orcid.org/0000-0001-8729-1530; Email: lbassett@seas.upenn.edu

Authors

Raj N. Patel − *Quantum Engineering Laboratory, Department of Electrical and Systems Engineering, University of Pennsylvania, Philadelphia, Pennsylvania 19104, United States;* Present Address: Nokia, 171 Madison Ave, RM 1100, New York, New York 10016, United States; orcid.org/0000-0003-1634-1208

Rebecca E. K. Fishman − *Quantum Engineering Laboratory, Department of Electrical and Systems Engineering, University of Pennsylvania, Philadelphia, Pennsylvania 19104, United States; Department of Physics and Astronomy, University of Pennsylvania, Philadelphia, Pennsylvania 19104, United States;* orcid.org/0000-0001-8271-7125

Tzu-Yung Huang − *Quantum Engineering Laboratory, Department of Electrical and Systems Engineering, University of Pennsylvania, Philadelphia, Pennsylvania 19104, United States;* Present Address: Nokia Bell Laboratories, 600 Mountain Ave., Murray Hill, New Jersey 07974, United States; orcid.org/0000-0001-9527-5581

Jordan A. Gusdorff − *Quantum Engineering Laboratory, Department of Electrical and Systems Engineering, University of Pennsylvania, Philadelphia, Pennsylvania 19104, United States; Department of Materials Science and Engineering, University of Pennsylvania, Philadelphia, Pennsylvania 19104, United States;* orcid.org/0000-0001-6609-2997

David A. Fehr − *Department of Physics and Astronomy, University of Iowa, Iowa City, Iowa 52242, United States*

David A. Hopper − *Quantum Engineering Laboratory, Department of Electrical and Systems Engineering, University of Pennsylvania, Philadelphia, Pennsylvania 19104, United States; Department of Physics and Astronomy, University of Pennsylvania, Philadelphia, Pennsylvania 19104, United States;* Present Address: imec, 220 Montgomery Street, Suite 1027, San Francisco, California 94104, United States; orcid.org/0000-0003-1965-690X

S. Alex Breitweiser − *Quantum Engineering Laboratory, Department of Electrical and Systems Engineering, University of Pennsylvania, Philadelphia, Pennsylvania 19104, United States; Department of Physics and Astronomy, University of Pennsylvania, Philadelphia, Pennsylvania 19104, United States;* Present Address: IBM Research, 1101 Kitchawan Rd., Yorktown Heights, NY 10598, United States; orcid.org/0000-0002-0325-4765

Benjamin Porat − *Quantum Engineering Laboratory, Department of Electrical and Systems Engineering, University of Pennsylvania, Philadelphia, Pennsylvania 19104, United States;* Present Address: Raytheon, 2000 E El Segundo Blvd., El Segundo, California 90245, United States

Michael E. Flatté − *Department of Physics and Astronomy, University of Iowa, Iowa City, Iowa 52242, United States; Department of Applied Physics, Eindhoven University of Technology, 5600 MB Eindhoven, The Netherlands*

Complete contact information is available at: https://pubs.acs.org/10.1021/acs.nanolett.4c01333

Author Contributions

#R.N.P. and R.E.K.F. contributed equally to this paper.

Notes

The authors declare no competing financial interest.

■ ACKNOWLEDGMENTS

This work was primarily supported by the National Science Foundation (NSF) award DMR-1922278 (Penn) and DMR-1921877 (Iowa). J.A.G. is supported by an NSF Graduate Research Fellowship (DGE-1845298). S.A.B. acknowledges support from an IBM Ph.D. Fellowship. The authors gratefully acknowledge use of facilities and instrumentation in the Singh Center for Nanotechnology at the University of Pennsylvania, supported by NSF through the National Nanotechnology Coordinated Infrastructure (NNCI; Grant ECCS-1542153) and the University of Pennsylvania Materials Research Science and Engineering Center (MRSEC; DMR-1720530). We gratefully acknowledge fruitful discussions with M. Turiansky and C. G. Van de Walle.

■ REFERENCES

(1) Aslam, N.; Pfender, M.; Neumann, P.; Reuter, R.; Zappe, A.; Favaro de Oliveira, F.; Denisenko, A.; Sumiya, H.; Onoda, S.; Isoya,

J.; Wrachtrup, J. Nanoscale nuclear magnetic resonance with chemical resolution. *Science* **2017**, *357*, 67−71.
(2) Degen, C. L.; Reinhard, F.; Cappellaro, P. Quantum sensing. *Rev. Mod. Phys.* **2017**, *89*, 035002.
(3) Block, M.; Kobrin, B.; Jarmola, A.; Hsieh, S.; Zu, C.; Figueroa, N. L.; Acosta, V. M.; Minguzzi, J.; Maze, J. R.; Budker, D.; Yao, N. Y. Optically Enhanced Electric Field Sensing Using Nitrogen-Vacancy Ensembles. *Physical Review Applied* **2021**, *16*, 024024.
(4) Abobeih, M. H.; Randall, J.; Bradley, C. E.; Bartling, H. P.; Bakker, M. A.; Degen, M. J.; Markham, M.; Twitchen, D. J.; Taminiau, T. H. Atomic-scale imaging of a 27-nuclear-spin cluster using a quantum sensor. *Nature* **2019**, *576*, 411−415.
(5) Hermans, S. L. N.; Pompili, M.; Beukers, H. K. C.; Baier, S.; Borregaard, J.; Hanson, R. Qubit teleportation between non-neighbouring nodes in a quantum network. *Nature* **2022**, *605*, 663−668.
(6) Bradley, C. E.; Randall, J.; Abobeih, M. H.; Berrevoets, R. C.; Degen, M. J.; Bakker, M. A.; Markham, M.; Twitchen, D. J.; Taminiau, T. H. A Ten-Qubit Solid-State Spin Register with Quantum Memory up to One Minute. *Physical Review X* **2019**, *9*, 031045.
(7) Stas, P.-J.; et al. Robust multi-qubit quantum network node with integrated error detection. *Science* **2022**, *378*, 557−560.
(8) Choi, S.; Choi, J.; Landig, R.; Kucsko, G.; Zhou, H.; Isoya, J.; Jelezko, F.; Onoda, S.; Sumiya, H.; Khemani, V.; von Keyserlingk, C.; Yao, N. Y.; Demler, E.; Lukin, M. D. Observation of discrete time-crystalline order in a disordered dipolar many-body system. *Nature* **2017**, *543*, 221−225.
(9) Wolfowicz, G.; Heremans, F. J.; Anderson, C. P.; Kanai, S.; Seo, H.; Gali, A.; Galli, G.; Awschalom, D. D. Quantum guidelines for solid-state spin defects. *Nature Reviews Materials* **2021**, *6*, 906−925.
(10) Bassett, L. C.; Alkauskas, A.; Exarhos, A. L.; Fu, K.-M. C. Quantum defects by design. *Nanophotonics* **2019**, *8*, 1867−1888.
(11) Aharonovich, I.; Tetienne, J.-P.; Toth, M. Quantum Emitters in Hexagonal Boron Nitride. *Nano Lett.* **2022**, *22*, 9227−9235.
(12) Baber, S.; Malein, R. N. E.; Khatri, P.; Keatley, P. S.; Guo, S.; Withers, F.; Ramsay, A. J.; Luxmoore, I. J. Excited State Spectroscopy of Boron Vacancy Defects in Hexagonal Boron Nitride Using Time-Resolved Optically Detected Magnetic Resonance. *Nano Lett.* **2022**, *22*, 461−467.
(13) Mathur, N.; Mukherjee, A.; Gao, X.; Luo, J.; McCullian, B. A.; Li, T.; Vamivakas, A. N.; Fuchs, G. D. Excited-state spin-resonance spectroscopy of VB- defect centers in hexagonal boron nitride. *Nat. Commun.* **2022**, *13*, 3233.
(14) Patel, R. N.; Hopper, D. A.; Gusdorff, J. A.; Turiansky, M. E.; Huang, T.-Y.; Fishman, R. E. K.; Porat, B.; Van de Walle, C. G.; Bassett, L. C. Probing the Optical Dynamics of Quantum Emitters in Hexagonal Boron Nitride. *PRX Quantum* **2022**, *3*, 030331.
(15) Guo, N.-J.; Li, S.; Liu, W.; Yang, Y.-Z.; Zeng, X.-D.; Yu, S.; Meng, Y.; Li, Z.-P.; Wang, Z.-A.; Xie, L.-K.; Ge, R.-C.; Wang, J.-F.; Li, Q.; Xu, J.-S.; Wang, Y.-T.; Tang, J.-S.; Gali, A.; Li, C.-F.; Guo, G.-C. Coherent control of an ultrabright single spin in hexagonal boron nitride at room temperature. *Nat. Commun.* **2023**, *14*, 2893.
(16) Exarhos, A. L.; Hopper, D. A.; Patel, R. N.; Doherty, M. W.; Bassett, L. C. Magnetic-field-dependent quantum emission in hexagonal boron nitride at room temperature. *Nat. Commun.* **2019**, *10*, 222.
(17) Gottscholl, A.; Kianinia, M.; Soltamov, V.; Orlinskii, S.; Mamin, G.; Bradac, C.; Kasper, C.; Krambrock, K.; Sperlich, A.; Toth, M.; Aharonovich, I.; Dyakonov, V. Initialization and read-out of intrinsic spin defects in a van der Waals crystal at room temperature. *Nat. Mater.* **2020**, *19*, 540−545.
(18) Chejanovsky, N.; Mukherjee, A.; Geng, J.; Chen, Y.-C.; Kim, Y.; Denisenko, A.; Finkler, A.; Taniguchi, T.; Watanabe, K.; Dasari, D. B. R.; Auburger, P.; Gali, A.; Smet, J. H.; Wrachtrup, J. Single-spin resonance in a van der Waals embedded paramagnetic defect. *Nat. Mater.* **2021**, *20*, 1079−1084.
(19) Stern, H. L.; Gu, Q.; Jarman, J.; Eizagirre Barker, S.; Mendelson, N.; Chugh, D.; Schott, S.; Tan, H. H.; Sirringhaus, H.; Aharonovich, I.; Atatüre, M. Room-temperature optically detected magnetic resonance of single defects in hexagonal boron nitride. *Nat. Commun.* **2022**, *13*, 618.
(20) Exarhos, A. L.; Hopper, D. A.; Grote, R. R.; Alkauskas, A.; Bassett, L. C. Optical Signatures of Quantum Emitters in Suspended Hexagonal Boron Nitride. *ACS Nano* **2017**, *11*, 3328−3336.
(21) Fishman, R. E. K.; Patel, R. N.; Hopper, D. A.; Huang, T.-Y.; Bassett, L. C. Photon-Emission-Correlation Spectroscopy as an Analytical Tool for Solid-State Quantum Defects. *PRX Quantum* **2023**, *4*, 010202.
(22) Jungwirth, N. R.; Calderon, B.; Ji, Y.; Spencer, M. G.; Flatte, M. E.; Fuchs, G. D. Temperature Dependence of Wavelength Selectable Zero-Phonon Emission from Single Defects in Hexagonal Boron Nitride. *Nano Lett.* **2016**, *16*, 6052−6057.
(23) Jungwirth, N. R.; Fuchs, G. D. Optical Absorption and Emission Mechanisms of Single Defects in Hexagonal Boron Nitride. *Phys. Rev. Lett.* **2017**, *119*, 057401.
(24) Ziegler, J.; Blaikie, A.; Fathalizadeh, A.; Miller, D.; Yasin, F. S.; Williams, K.; Mohrhardt, J.; McMorran, B. J.; Zettl, A.; Aleman, B. Single-Photon Emitters in Boron Nitride Nanococoons. *Nano Lett.* **2018**, *18*, 2683−2688.
(25) Doherty, M. W.; Manson, N. B.; Delaney, P.; Jelezko, F.; Wrachtrup, J.; Hollenberg, L. C. L. The nitrogen-vacancy colour centre in diamond. *Phys. Rep.* **2013**, *528*, 1−45.
(26) Epstein, R. J.; Mendoza, F. M.; Kato, Y. K.; Awschalom, D. D. Anisotropic interactions of a single spin and dark-spin spectroscopy in diamond. *Nat. Phys.* **2005**, *1*, 94−98.
(27) Berthel, M.; Mollet, O.; Dantelle, G.; Gacoin, T.; Huant, S.; Drezet, A. Photophysics of single nitrogen-vacancy centers in diamond nanocrystals. *Phys. Rev. B* **2015**, *91*, 035308.
(28) Frantsuzov, P.; Kuno, M.; Janko, B.; Marcus, R. A. Universal emission intermittency in quantum dots, nanorods and nanowires. *Nat. Phys.* **2008**, *4*, 519−522.
(29) Breuer, H.-P.; Petruccione, F. *The Theory of Open Quantum Systems*; Oxford University Press, 2007.
(30) Hopper, D. A.; Shulevitz, H. J.; Bassett, L. C. Spin readout techniques of the nitrogen-vacancy center in diamond. *Micromachines* **2018**, *9*, 437.
(31) Lee, S.-Y.; Widmann, M.; Rendler, T.; Doherty, M. W.; Babinec, T. M.; Yang, S.; Eyer, M.; Siyushev, P.; Hausmann, B. J. M.; Loncar, M.; Bodrog, Z.; Gali, A.; Manson, N. B.; Fedder, H.; Wrachtrup, J. Readout and control of a single nuclear spin with a metastable electron spin ancilla. *Nat. Nanotechnol.* **2013**, *8*, 487−492.

https://doi.org/10.1021/acs.nanolett.4c01333
Nano Lett. 2024, 24, 7623−7628